

A Submillimeter View of Circumstellar Dust Disks in ρ Ophiuchus

Sean M. Andrews¹ and Jonathan P. Williams

Institute for Astronomy, University of Hawaii, 2680 Woodlawn Drive, Honolulu, HI 96822

andrews@ifa.hawaii.edu, jpw@ifa.hawaii.edu

ABSTRACT

We present new multiwavelength submillimeter continuum measurements of the circumstellar dust around 48 young stars in the ρ Ophiuchus dark clouds. Supplemented with previous 1.3 mm observations of an additional 99 objects from the literature, the statistical distributions of disk masses and submillimeter colors are calculated and compared to those in the Taurus-Auriga region. These basic submillimeter properties of young stellar objects in both environments are shown to be essentially identical. As with their Taurus counterparts, the ρ Oph circumstellar dust properties are shown to evolve along an empirical evolution sequence based on the infrared spectral energy distribution. The combined ρ Oph and Taurus Class II samples (173 sources) are used to set benchmark values for basic outer disk characteristics: $M_d \sim 0.005 M_\odot$, $M_d/M_* \sim 1\%$, and $\alpha \sim 2$ (where $F_\nu \propto \nu^\alpha$ between $350 \mu\text{m}$ and 1.3mm). The precision of these numbers are addressed in the context of substantial solid particle growth in the earliest stages of the planet formation process. There is some circumstantial evidence that disk masses inferred from submillimeter emission may be under-estimated by up to an order of magnitude.

Subject headings: circumstellar matter — planetary systems: protoplanetary disks — solar system: formation — stars: pre-main—sequence

1. Introduction

Circumstellar accretion disks are an integral part of the star and planet formation process. They are critical for conserving angular momentum during molecular cloud core collapse (Terebey et al. 1984), channeling mass onto the central star (Lynden-Bell & Pringle 1974), and assembling raw material into a planetary system (e.g., Lissauer & Stevenson 2007). The structural, material, and chemical compositions of disks provide crucial insights on the initial conditions of the planet formation process. While molecular gas is the dominant mass species in these disks, observations of this phase are notoriously difficult due to the radiative inefficiency of H_2 , the depletion of molecules

¹Present address: Harvard-Smithsonian Center for Astrophysics, 60 Garden Street, MS 42, Cambridge, MA 02138

from the gas phase onto dust grain surfaces, and the relative insensitivity of many current telescopes. Consequently, much of our knowledge of disk properties is gathered from the comparatively bright thermal continuum emission of dust particles heated by irradiation from the central star (see Natta et al. 2007).

At any given frequency, this continuum emission is generated from dust grains at a relatively small range of contributing stellocentric radii (e.g., Beckwith et al. 1990). Therefore, the detailed morphology of its spectral energy distribution (SED) is dictated by the physical structure and material content of the disk (e.g., temperatures, densities, geometry, and particle properties). Much of the infrared SED is generated in the optically thick inner few AU of the disk, corresponding roughly to the region in the Solar System occupied by the terrestrial planets. Because optical depths are so high at these radii, the infrared SED can be used to infer disk temperatures (e.g., Adams et al. 1987; Chiang & Goldreich 1997; D’Alessio et al. 1998). The far-infrared and millimeter/radio portion of the SED (hereafter referred to as “submillimeter” for convenience) originates primarily in the optically thin outer disk, from several to perhaps hundreds of AU. The low column densities in this region lead to a direct relationship between the submillimeter luminosity and the disk mass (Hildebrand 1983; Beckwith et al. 1990; André & Montmerle 1994). Moreover, the shape of the long-wavelength SED is at least partially controlled by the disk opacity (Beckwith & Sargent 1991; Mannings & Emerson 1994). The optical properties of the dust grain population, especially the particle size distribution, are encoded in this latter parameter (Pollack et al. 1994; Draine 2006).

In practice, one can infer the circumstellar dust mass around a young star with a submillimeter flux density and constrain the bulk optical characteristics of the solid particle population using submillimeter colors. Constraints on these properties are empirical prerequisites for understanding the mechanisms and timescales involved in the planet formation process. The progenitor disk mass not only sets a limit on the material composition and structure of a potential planetary system, but can also elucidate whether any particular mechanism of planet formation is more plausible than another. As an example, models that rely on gravitational instabilities in the disk to drive rapid giant planet formation are only tenable if the disk is sufficiently massive (Boss 1998; Mayer et al. 2007). Moreover, interpreting submillimeter colors in terms of the current solid particle size distribution in these disks may reveal clues on the efficiency of the grain growth process, representing the first tentative steps of building planetesimals.

Beckwith et al. (1990) presented the first large survey of the 1.3 mm emission from young stellar objects (YSOs; defined here as a young star and its circumstellar environment) in the Taurus-Auriga star formation region. Following up with a supplementary survey (Osterloh & Beckwith 1995) and smaller, multiwavelength submillimeter samples (Beckwith & Sargent 1991; Mannings & Emerson 1994), these studies provided the first detailed look at the circumstellar disk mass distribution and the shape of the opacity spectrum. The results argued for a typical disk mass similar to that required to form the Solar System and an opacity spectrum shallower than noted in the interstellar medium (ISM), possibly due to grain growth. Around the same time, André & Montmerle (1994) built on their previous work (André et al. 1990) with a pioneering investigation of the millimeter

continuum emission from YSOs in the ρ Ophiuchus dark clouds. One major impact of their work was highlighting that the millimeter luminosities appeared tied to the same YSO evolution sequence typically tracked in the infrared: younger sources on this empirical sequence were shown to have larger circumstellar dust masses.

To build on these landmark studies while taking advantage of technological advancements in the sensitivity and efficiency of submillimeter detectors, we undertook a comprehensive, deep, multiwavelength survey of Taurus YSOs (Andrews & Williams 2005, hereafter Paper I). Centered around an $850\ \mu\text{m}$ sample of ~ 150 sources, this work had the benefits of at least a factor of 5 better sensitivity and a considerably more uniform luminosity limit than previous observations. In addition to a more complete census of disk masses and their evolution, this survey permitted us to derive the distribution of submillimeter colors between $350\ \mu\text{m}$ and $1.3\ \text{mm}$, and show that these also changed as a function of YSO evolutionary state. In this article, we present a similar study of the submillimeter continuum emission from circumstellar dust in the ρ Oph region. In §2 we describe the new survey data, its acquisition and reduction, and the compilation of an extended sample similar to the one used for Taurus. Disk masses and colors are computed in §3, and the results for ρ Oph YSOs are systematically compared with their counterparts in Taurus. Potential relationships of these properties with evolutionary diagnostics, stellar host parameters, and the planet formation process are discussed in §4, before concluding with a summary in §5.

2. Observations and Data Reduction

The Submillimeter Common-User Bolometer Array (SCUBA: Holland et al. 1999) instrument at the 15 m James Clerk Maxwell Telescope (JCMT) was used to observe 48 ρ Oph YSOs during two runs in 2004 April and 2005 June. The observations were conducted in photometry mode, providing simultaneous measurements of the 450 and $850\ \mu\text{m}$ continuum emission within FWHM beam diameters of $9''$ and $14''$, respectively. Pointing centers accurate to $< 1\%$ of the beam size were determined from the Two Micron All Sky Survey (2MASS) Point Source Catalog (Cutri et al. 2003). The typical precipitable water vapor level during the observations was $\lesssim 1.8\ \text{mm}$, corresponding to zenith optical depths of $0.3\text{--}0.4$ at $850\ \mu\text{m}$ and ~ 2 at $450\ \mu\text{m}$. The same observing and data reduction strategies described in detail in Paper I were utilized for this sample. The systematic uncertainties associated with absolute flux calibration are expected to be $\sim 10\%$ and 25% for 850 and $450\ \mu\text{m}$, respectively.

Images of the $350\ \mu\text{m}$ continuum for 7 YSOs were obtained with the Submillimeter High Angular Resolution Camera (SHARC-II: Dowell et al. 2003) on the 10 m Caltech Submillimeter Observatory (CSO) telescope in 2004 March and June. As with the SHARC-II observations described in Paper I, these diffraction-limited images (FWHM beam diameter of $9''$) were obtained by constantly scanning the telescope in the vicinity of the source in a Lissajous pattern. Further details on the observing technique and data reduction are highlighted in Paper I. The absolute flux calibration of these $350\ \mu\text{m}$ data is accurate to $\sim 25\%$.

Unfortunately, the large submillimeter photometry survey of ρ Oph YSOs that was originally planned was cut short by the de-commissioning of SCUBA in the summer of 2006. For a more complete sample of ρ Oph similar in size and content to that presented in Paper I for Taurus, the data described above were supplemented with a large number of 1.3 mm single-dish observations from the literature (André & Montmerle 1994; Jensen et al. 1996; Nürnberger et al. 1998; Motte et al. 1998; Stanke et al. 2006). This expanded sample consists of 147 objects; 48 with multiwavelength data, and 99 others with only 1.3 mm flux densities from previous work. The vast majority of the sources lie in the L1688 dark cloud, with a few others scattered in L1689 and the surrounding Oph-Sco complex. Table 1 lists the 350, 450, 850, and 1300 μm flux densities for these 147 sources, along with disk masses (§3.1), submillimeter colors (§3.2), and other relevant properties. Figure 1 summarizes some of the basic characteristics of the ρ Oph sample.

In what follows, we follow Wilking et al. (2005) and adopt a distance of 150 pc to ρ Oph. For this distance, the projected FWHM beam sizes are 1350 AU for both 350 and 450 μm and 2100 AU for 850 μm . Because these single-dish beams are substantially larger than the circumstellar dust associated with Class II and III sources (e.g., Kitamura et al. 2002; Andrews & Williams 2007), it is safe to assume that the values listed in Table 1 for such objects represent the total integrated continuum flux densities. As shown in mapping observations (e.g., Motte et al. 1998; Stanke et al. 2006) and discussed in Paper I, this is not likely the case for Class I sources. It is important to emphasize that the photometry for the Class I YSOs listed in Table 1 corresponds to the combined continuum emission contributions from both a circumstellar disk and the inner regions of a circumstellar envelope.

3. Results

3.1. Disk Masses

Following our work in Paper I, we aim to provide some empirical calibration of the relationship between submillimeter luminosities and disk masses through the use of a simple disk structure model. A geometrically thin irradiated dust disk emits thermal radiation modified by the optical properties of the solid particles from a continuous series of annuli at a range of stellocentric radii. The SED of this emission at a given frequency ν (here defined as $L_\nu = 4\pi d^2 \nu F_\nu$) can be described in terms of the physical conditions in the disk as

$$L_\nu = 8\pi^2 \nu \cos i \int_{r_0}^{R_d} B_\nu(T_r) (1 - e^{-\tau_{\nu,r} \sec i}) r dr, \quad (1)$$

where i is the disk inclination, r_0 and R_d the inner and outer radii, $B_\nu(T_r)$ the Planck function at a radius-dependent temperature, and $\tau_{\nu,r}$ the optical depth of the disk material (e.g., Adams et al. 1987; Beckwith et al. 1990; Chiang & Goldreich 1997). The latter is taken to be the product of the opacity, κ_ν , and surface density, Σ_r . The disk structure is approximated with radial power-laws, where $T_r \propto r^{-q}$ and $\Sigma_r \propto r^{-p}$. To simplify the SED modeling process, we define the opacity to have

a spatially homogeneous power-law spectrum such that $\kappa_\nu \propto \nu^\beta$ with $\beta = 1$ and a normalization of $\kappa_0 = 0.1 \text{ cm}^2 \text{ g}^{-1}$ at 1000 GHz (cf., Beckwith et al. 1990). This opacity implicitly assumes a 100:1 mass ratio of gas to dust.

We identified a subsample of 19 ρ Oph YSOs that had suitable mid-infrared through millimeter SED data in the literature to determine M_d from a fit to this simple disk structure model. For consistency with the work done in Paper I for Taurus sources, we fixed the following parameters in the SED modeling of this subsample: $i = 0^\circ$, $r_0 = 0.01 \text{ AU}$, $R_d = 100 \text{ AU}$, and $p = 1.5$. The SEDs longward of $5 \mu\text{m}$ were de-reddened (see §4.2) and fit to the model using χ^2 -minimization. The results of the SED fits are compiled in Table 2, including literature sources for the SED data, the reduced χ^2 statistic, degrees of freedom in the fit, and the best-fit values for the 3 free model parameters; T_1 (the temperature at 1 AU), q (the radial power-law index of the temperature profile), and M_d (determined from the surface density profile and fixed outer radius).

Using these results and their counterparts for the Taurus sample (see Paper I), Figure 2 demonstrates that the submillimeter flux densities and best-fit disk masses are correlated. Most of the YSOs do not have sufficient data to determine M_d from a SED fit, and therefore an alternative method is required. As discussed in the introduction, most disks are primarily optically thin at submillimeter wavelengths (Beckwith et al. 1990). Assuming that $\tau_{\nu,r} \ll 1$ and the emission is generated in a roughly isothermal region with a characteristic temperature (T_c), Eqn. 1 reduces to

$$L_\nu \approx 8\pi^2 \nu \kappa_\nu B_\nu(T_c) M_d. \quad (2)$$

This approximation explicitly shows that the submillimeter luminosity is a direct diagnostic of the total optical depth in the disk, or the product $\kappa_\nu M_d$. The behavior of this simplified relationship is able to reproduce the SED fit results for both Taurus and ρ Oph YSOs quite well in Figure 2, where it is plotted as a solid line for $T_c = 20 \text{ K}$.

The disk masses (or upper limits) for the remaining 128 YSOs in this sample without sufficient SED data were computed according to Eqn. 2 with a characteristic temperature of 20 K. These M_d values are compiled in Table 1, with preference given to using the more modern and sensitive $850 \mu\text{m}$ flux densities when available. The resulting cumulative distribution of ρ Oph disk masses for the full sample is shown in Figure 3, constructed with the Kaplan-Meier product-limit estimator to incorporate the upper limits (Feigelson & Nelson 1985; see also e.g., Paper I or André & Montmerle 1994). This distribution (and others like it in what follows) shows the probability that a given disk in the sample has a mass greater than or equal to the abscissa value. The median disk mass in the full ρ Oph sample is $\langle M_d \rangle \approx 0.002 M_\odot$. Roughly 28% of these sources have $M_d \geq 0.01 M_\odot$, a representative value for the minimal amount of solar-composition material required to account for the planets in the Solar System (the Minimum Mass Solar Nebula, hereafter MMSN; Weidenschilling 1977). Only 40% of the ρ Oph YSOs have $M_d \lesssim 0.001 M_\odot$, corresponding to the mass of Jupiter.

3.2. Submillimeter Colors

The submillimeter continuum spectra of YSOs generally follow a simple power-law behavior, such that $F_\nu \propto \nu^\alpha$. The spectral index α is essentially a submillimeter color, and potentially encapsulates important information about the optical properties of solid particles in the disk. For the optically thin, isothermal approximation (Eqn. 2), the submillimeter continuum emission has a spectral dependence $L_\nu \propto \nu^3 \kappa_\nu \propto \nu^{3+\beta}$ in the Rayleigh-Jeans limit (Beckwith et al. 1990; Beckwith & Sargent 1991). With these assumptions, the submillimeter color is directly related to the shape of the opacity spectrum, $\alpha = 2 + \beta$, which in turn is thought to be a composite diagnostic of the dust particle size distribution, mineralogical composition, and morphology (e.g., Miyake & Nakagawa 1993; Henning & Stognienko 1996; Draine 2006). In the ISM, the generally small (sub-micron) dust particles are relatively inefficient submillimeter emitters with $\beta \approx 1.7$ (e.g., Li & Draine 2001), resulting in steep submillimeter spectra with $\alpha \approx 4$ (e.g., Hildebrand 1983). However, in the high-density environment of a circumstellar disk, solid particles are expected to grow to substantially larger sizes via collisional agglomeration (see the recent review by Dominik et al. 2007). For a given grain composition and morphology, increased particle sizes due to such growth will decrease the value of β (e.g., Miyake & Nakagawa 1993; Draine 2006). This in turn would be manifested as a shallow submillimeter continuum spectrum, or decreased α .

To assess the potential signatures of grain growth in ρ Oph disks, we have calculated submillimeter colors (α) between $350 \mu\text{m}$ and 1.3mm whenever multiwavelength data were available. In cases with >2 flux density measurements in this wavelength range, α was determined by a linear fit in the $\{\log \nu, \log F_\nu\}$ plane. Otherwise, a simple flux ratio was utilized to measure a color or upper limit. The inferred values of α are included in Table 1. Figure 4 shows their cumulative distribution, again constructed with the Kaplan-Meier estimator to include upper limits. The median value is $\langle \alpha \rangle \approx 2$, with only a few percent of the YSOs showing $\alpha \geq 3$.

Based on the above discussion, it would be tempting to conclude that the submillimeter SEDs for the ρ Oph sample show clear evidence for significant solid particle growth (with $\beta \lesssim 1$). However, there are a number of other effects that can serve to mimic the signatures of a shallow opacity spectrum. Perhaps the most relevant of these is optically thick contamination, originating in the dense inner disk. As a tracer of the disk temperature, emission with large optical depths will bias α to lower values because it has the same spectral shape as the Planck function in the Rayleigh-Jeans limit ($\alpha = 2$). Interferometric observations that resolve the disk structure can be used to quantify the contamination, and usually indicate optically thick fractions of $\lesssim 20 - 30\%$ shortward of 1mm (e.g., Testi et al. 2001, 2003; Andrews & Williams 2007). Moreover, the presumed origin of the submillimeter continuum emission near the cold disk midplane (e.g., Chiang & Goldreich 1997; Dullemond et al. 2002) implies that the Rayleigh-Jeans limit may not be valid (i.e., if much of the emission comes from dust with $T \lesssim 15 \text{K}$). In this case, the thermal emission is considerably shallower than ν^2 and may contribute to the observed low α values. Finally, there are more technical considerations, particularly the rather large uncertainties on α due to calibration inaccuracies and small frequency leverage, as well as contamination from non-disk emission (see Paper I for details).

Despite these uncertainties, it would be difficult to account for the submillimeter color distribution in Figure 4 for an opacity spectrum similar to that in the ISM (see D’Alessio et al. 2001). Detailed disk structure modeling and spatially resolved data are required to reach a more definitive conclusion. In those cases where the disk structure has been resolved and can be used to correct the colors (α) for optically thick contamination, the typical opacity index is $\beta \approx 1$ (Testi et al. 2001, 2003; Rodmann et al. 2006; Lommen et al. 2007; Andrews & Williams 2007). Without resolved data, the colors presented here serve solely as empirical properties of YSOs. While the opacity spectra of these sources remain uncertain, the observed colors are certainly significantly different than noted for dust in the ISM, in the same sense as expected for when particle sizes are increased. The issue of grain growth will be addressed further in §4.3.

3.3. A Comparison with Disks in Taurus-Auriga

Having established the basic submillimeter properties of YSOs in ρ Oph, we can make a comparison with their counterparts in Taurus from Paper I. Taurus is a substantially less crowded region, with projected stellar densities reaching only $\sim 50\text{--}60$ stars pc^{-2} (Gomez et al. 1993) compared with the ~ 200 stars pc^{-2} noted in the ρ Oph core (Greene & Young 1992). Despite the higher concentration of YSOs in ρ Oph, a simple calculation of the collision timescale shows that dynamical interactions are not expected to significantly affect their disk properties. De-projecting the Greene & Young (1992) stellar density into a 1 pc^3 volume ($n_* \sim 200 \text{ pc}^{-3}$) and assuming a typical disk size ($r \sim 100 \text{ AU} \Rightarrow \sigma \sim 10^{-8} \text{ pc}^{-2}$, where σ is the collisional cross section) and cluster velocity dispersion ($v \sim 1 \text{ km s}^{-1}$) implies a disk–disk collision timescale of $t_c \approx (n_*\sigma v)^{-1} \sim 1 \text{ Gyr}$, roughly 3 orders of magnitude larger than the cluster lifetime.

In addition to being more spatially concentrated, ρ Oph members are often still deeply embedded in their natal molecular cloud material. This is in stark contrast to most YSOs in the Taurus association, which by comparison are relatively unobscured. Given these environmental distinctions, it is worthwhile to examine if they have any impact on disk properties by directly comparing the results for the two regions.

To make the comparison a fair one, most of the Taurus disk masses were re-calculated from the $850 \mu\text{m}$ flux densities in Paper I using Eqn. 2, the same parameters adopted here (see §3.1), and the appropriate distance, $d = 140 \text{ pc}$. A subsample of Taurus sources have sufficient information to determine M_d from a fit to the full SED (see Table 2 in Paper I), and in those cases the best-fit disk masses were adopted. Direct comparisons of the cumulative distribution functions of M_d and α for the similar-sized (~ 150 YSOs) ρ Oph and Taurus samples are shown in the top panels of Figure 5. These distribution functions take into account upper limits using the Kaplan-Meier estimator and should be a reliable comparison for $M_d \gtrsim 0.001 M_\odot$, corresponding to a rough luminosity limit for the ρ Oph sample. The error envelopes of the Taurus distributions are shown in grayscale and the ρ Oph distributions as histograms with error bars. The two-sample statistical tests described in the survival analysis formalism of Feigelson & Nelson (1985, i.e., the Gehan, Logrank, Peto &

Peto, and Peto & Prentice tests) confirm what is apparent from Figure 5: the distributions of M_d and α for ρ Oph and Taurus YSOs are essentially indistinguishable. The results of these tests are provided in the top half of Table 3.

Since the relative numbers of YSOs in various evolutionary states are not the same in the ρ Oph and Taurus samples, a closer look at more similar subsamples makes a better comparison. The shape of the infrared SED is often utilized as an empirical diagnostic of the YSO evolution sequence (Lada & Wilking 1984; Adams & Shu 1986; Adams et al. 1987). The parameter of interest is the SED index n , defined from $\sim 2\text{--}25\ \mu\text{m}$ via $\nu F_\nu \propto \nu^n$. We adopt the classification breakdown suggested by Greene et al. (1994), where Class I objects (star+disk+envelope) have $n \leq -0.3$, Flat-Spectrum objects (star+disk+envelope?) have $-0.3 < n < 0.3$, Class II objects (star+disk) have $0.3 \leq n \leq 1.6$, and Class III objects (star only) have $n > 1.6$. Infrared photometry for the ρ Oph sample was collected from the literature (Wilking et al. 1989; Weaver & Jones 1992; Greene et al. 1994; Bontemps et al. 2001; Barsony et al. 2005; Padgett et al. 2006), the 2MASS Point Source Catalog (Cutri et al. 2003), and the preliminary results of the ‘‘Cores to Disks’’ *Spitzer* Legacy Survey of the region (L. Allen 2007, private communication). The infrared photometry of Taurus sources utilized for this same purpose in Paper I was supplemented with *Spitzer* photometry from Hartmann et al. (2005) and Luhman et al. (2006). Infrared SED slopes (n) were computed for each YSO in the ρ Oph and Taurus samples with a simple power-law fit to the SED, corrected for reddening whenever possible (extinctions were computed as described in §4.2 or Paper I). The resulting SED classifications for the ρ Oph sample are included in Table 1.

This empirical evolution sequence was used to generate YSO subsamples in both star-forming environments and compare them with the aforementioned two-sample statistical tests. The results are compiled in the top portion of Table 3, and the cumulative distributions of M_d and α for various SED classifications are also shown in Figure 5. The P values in Table 3 correspond to the probability that the two subsamples are drawn from *different* parent distributions. The ranges of P represent the various statistical tests (see Feigelson & Nelson 1985). After concluding that the few Flat-Spectrum sources do not substantially influence the results (as was noted in Paper I), they were incorporated into the Class II subsample.

Although not significant by formal statistical arguments, the distributions of M_d and α for Class I objects in the two regions appear somewhat different in Figure 5. Little import should be attached to this apparent discrepancy, as the photometry has not been conducted in a systematic way and the potential for different amounts of envelope contamination has therefore not been properly taken into account. On the other hand, the level of detail in the agreement between the ρ Oph and Taurus distributions of M_d and α for Class II sources is remarkable. For disk masses greater than $\sim 0.001\ M_\odot$, the distributions between the two regions are essentially identical, even showing the same dip feature around the MMSN value ($0.01\ M_\odot$) and decrease to virtually zero probability for disks with $M_d \gtrsim 0.1\ M_\odot$. The median Class II disk in both samples has $\langle M_d \rangle \approx 0.005\ M_\odot$, with roughly one third of each sample harboring disks with $M_d \geq M_{\text{MMSN}}$. The shapes of the submillimeter color distributions between the two regions are also fairly precise

matches, with median values $\langle\alpha\rangle \approx 2$ and only a few percent of each sample having $\alpha \geq 3$.

As with the full samples, the subsamples described above indicate that there are no statistically significant differences between the submillimeter properties of YSOs in the ρ Oph and Taurus regions at *any given evolutionary state*. Given the roughly equivalent sizes and basic characteristics of the samples in these two regions and the homogeneous methodology utilized to infer M_d and α , this result clearly indicates that the local environment of a low-mass, low stellar density ($\ll 10^3$ stars pc^{-2}) region does not substantially affect the submillimeter properties of the associated disks.

4. Discussion

4.1. Disk Evolution

While confirming the similarities between the submillimeter properties of circumstellar dust in the ρ Oph and Taurus regions, the panels in Figure 5 also show that there are substantial changes in M_d and α across the empirical evolution sequence characterized by the infrared SED index. Two-sample tests on the censored datasets directly confirm that the M_d distributions of Class I, II, and III sources in ρ Oph are statistically different. The test results are catalogued in the bottom half of Table 3. As with the YSOs in the Taurus clouds (Paper I), submillimeter luminosities (and therefore disk masses) and colors decrease substantially along the Class I \rightarrow II \rightarrow III sequence.

Figure 6 directly demonstrates how the disk masses and submillimeter colors vary as a function of the infrared SED index (n), now combining the data for the ρ Oph and Taurus samples. The top panel reinforces what is seen in the left panels of Figure 5: M_d decreases as the infrared SED becomes bluer (i.e., n increases) along the evolution sequence. Using only the detections, a correlation between M_d and n is present at the 4σ level, with a Spearman rank correlation coefficient of -0.32 . The correlation significance is enhanced when the upper limits are incorporated with any of the survival analysis statistics discussed by Isobe et al. (1986). Disk masses decrease smoothly with a shallow slope for YSOs with infrared SEDs redward of the Class II/III boundary (at $n \sim 1.6$), but then drop precipitously. This non-linear behavior in the $\{n, M_d\}$ -plane was in fact originally postulated in the pioneering study by André & Montmerle (1994), along with the first indications that the ρ Oph and Taurus disk mass distributions were the same. In an effort to approximately determine the depth of the drop-off beyond the Class III boundary, we stacked the $850\ \mu\text{m}$ SCUBA photometry observations of all undetected Class III sources in ρ Oph and Taurus (Paper I) to derive their average luminosity value (see, e.g., Carpenter 2002). The mean $850\ \mu\text{m}$ flux density for the 54 stacked Class III non-detections (5 in ρ Oph and 49 in Taurus) was 0.1 ± 0.3 mJy. With the same assumptions adopted in §3.1, the 3σ “average” limit (0.9 mJy) indicates that the typical undetected Class III source has $M_d \lesssim 5 \times 10^{-5} M_\odot$, roughly the mass of Neptune.

The bottom panel in Figure 6 examines the comparative evolution of colors in the infrared and submillimeter bands. There is a marginal (2.9σ) correlation between α and n in this diagram

with a Spearman rank correlation coefficient of -0.30 , suggesting that α systematically decreases along the infrared evolution sequence. A similar correlation for the Taurus sources alone was noted in Paper I, and there partially attributed to a genuinely evolving disk opacity. The idea behind this argument is that disks are expected to become more optically thin as YSOs evolve along the infrared SED sequence. In the case of no opacity evolution, a decreasing fraction of optically thick submillimeter emission as n increases should lead to increasing α , the opposite of what is noted in Figure 6. On the other hand, the growth of solid particles as the circumstellar dust evolves along the sequence would result in a flattening of the opacity spectrum (decreased β), and therefore the observed decreasing α . An alternative (or possibly cooperative) scenario could be a decreasing temperature in the disk midplane (e.g., due to gravitational sedimentation of dust to the disk midplane; D’Alessio et al. 2006). These possibilities can potentially be explored with spatially resolved multiwavelength data, although with such a weak correlation many more sources would need to be observed with interferometers.

The above analysis confirms for ρ Oph what was shown for Taurus in Paper I: the infrared and submillimeter properties of circumstellar dust around young stars evolve along a similar empirical sequence. Given where such emission originates, this result suggests that the material in the inner (infrared) and outer (submillimeter) parts of disks is significantly affected by global changes in disk properties. One of the obvious candidates for the cause of such evolution is the metamorphosis of circumstellar structure, including the dissipation of the envelope (Class I \rightarrow II), the viscous evolution of the accretion disk (through Class II), and the dissipation of the disk (Class II \rightarrow III). A perhaps equally important contribution to this evolution could be the result of the substantial growth of solid particles. In reality, the submillimeter luminosity is determined by the product $\kappa_\nu M_d$: even if the total circumstellar mass remained the same across the evolution sequence, the observed trends could both be explained by the changes in the opacity expected from grain growth.

Given the abruptness of the transition at the Class II/III boundary in the top panel of Figure 6 and the low submillimeter detection rate for Class III sources (see also Paper I), it appears that the signatures of the inner and outer disk (infrared and submillimeter excesses, respectively) disappear within a short time of one another. In Paper I, we used the standard “duty-cycle” argument for this based on the very small percentage ($\lesssim 3\%$) of YSOs that have long-wavelength (i.e., submillimeter) emission from the outer disk, but no near-infrared excess from the inner disk. The scarcity of such “transition” objects suggests that if all disks go through such a phase, it must be rather short in duration ($\leq 10^5$ yr). A variety of mechanisms have been proposed for this rapid radial evolution, from planet formation (see Najita et al. 2007, and references therein) to rapid mass loss in photoevaporative winds (Clarke et al. 2001; Alexander et al. 2006).

4.2. Relation to Stellar Properties

Despite the above effort to associate changes in the submillimeter properties of circumstellar dust with an empirical evolution sequence, it is still not possible to tie this sequence to an abso-

lute timeframe. An alternative examination of disk evolution can be made by relating disk and stellar parameters, particularly masses (M_*) and ages (t_*). To determine the latter, we first collected spectral classifications (see Table 1) and optical/near-infrared photometry from the literature (Rydgren 1980; Chini 1981; Myers et al. 1987; Herbig & Bell 1988; Bouvier & Appenzeller 1992; Vrba et al. 1993; Herbst et al. 1994; Greene & Meyer 1995; Luhman & Rieke 1999; Wilking et al. 1999; Chavarría et al. 2000; Prato et al. 2003; Doppmann et al. 2003, 2005; Eisner et al. 2005; Wilking et al. 2005; Gras-Velázquez & Ray 2005; Padgett et al. 2006; Grankin et al. 2007). For sources in the surveys of Wilking et al. (2005) or Doppmann et al. (2003, 2005), we simply adopted their stellar masses and ages. For the remainder of the sample, we used the spectral type–effective temperature scale, intrinsic colors, and bolometric corrections tabulated by Kenyon & Hartmann (1995). Visual extinctions were calculated from color excesses (in the optical-red whenever available) and the Cohen et al. (1981) extinction law. Stellar luminosities were then computed from the de-reddened photometry and appropriate bolometric correction. Stellar masses and ages were determined by reference to the D’Antona & Mazzitelli (1997) theoretical pre–main-sequence mass tracks and isochrones in an H-R diagram.

This is the same technique adopted for the Taurus YSOs in Paper I, and is similar in practice to that utilized by Wilking et al. (2005). The stellar mass and age distributions were already highlighted in Figure 1. The ρ Oph sample is slightly younger than the Taurus sample, with a median age of ~ 0.7 Myr compared to ~ 1 Myr. The cumulative distributions of disk-to-star mass ratios (M_d/M_*) for Class II sources in both the ρ Oph (lines) and Taurus (grayscale) samples are shown together in Figure 7. The ρ Oph sources generally exhibit slightly higher mass ratios than their Taurus counterparts, although the M_d/M_* distributions for the two regions are not formally different in a statistical sense. The median ratio in ρ Oph is $\langle M_d/M_* \rangle \approx 1.0\%$, compared to $\sim 0.8\%$ for Taurus. In this case, selection effects may be mimicking a subtle diagnostic of disk evolution from the slightly younger ρ Oph sample to the more mature Taurus YSOs. The ρ Oph sample does have a somewhat different M_* distribution, suggesting that any true hint of a change in M_d/M_* as a function of cluster age should await larger samples with more similarity in their stellar properties.

Figure 8 exhibits the variations of M_d , M_d/M_* , and α with time for the combined ρ Oph and Taurus sample. While there is a large scatter of disk properties at any given time, some marginal trends are apparent. Although a definitive correlation between M_d and t_* remains unconfirmed, there are clearly more non-detections as the stars get older. Using survival analysis techniques to incorporate upper limits, the Cox proportional hazard model, generalized Kendall’s tau, and Spearman’s rho correlation tests (Isobe et al. 1986) all suggest that the disk-to-star mass ratio is indeed correlated with the stellar age, dropping from a few percent at ~ 0.1 Myr to a factor of 30 or more lower by 10 Myr. It would be useful to measure disk masses for clusters with slightly *older* ages to confirm such trends, so that the strength of the correlation does not hinge on the youngest sources (i.e., $t \lesssim 10^5$ yr), where the isochrones are less trustworthy. No obvious trend between α and age is apparent.

Before moving on, it is worthwhile to comment on the adopted distance ($d = 150$ pc) and how

alternative values would be expected to affect the above analysis. Following Wilking et al. (2005) and others, we based the choice of d on the typical range of $\sim 130\text{--}170$ pc from measurements of stars in the larger Upper Scorpius complex that encompasses the ρ Oph clouds (e.g., Whittet 1974; de Geus et al. 1989; Knude & Høg 1998; de Zeeuw et al. 1999; Mamajek 2007). However, other authors have focused on the near end of that range, using the $d = 125$ pc advocated by de Geus and colleagues based on two arguments suggesting that the dark clouds are in the Upper Sco foreground: (a) the morphology of the distance modulus vs. extinction diagram for Upper Sco sources near the ρ Oph cloud edge (de Geus et al. 1989), and (b) some circumstantial evidence from the morphology of the local ISM (de Geus & Burton 1992).

If this closer distance is adopted, all luminosities utilized above are reduced by $\sim 30\%$, with two important consequences. First, the decreased bolometric luminosities in the H-R diagram would result in considerably older ages for the ρ Oph sample (stellar masses would remain approximately the same, owing to the essentially vertical tracks in this diagram). With the roughly logarithmic behavior of isochrones along the H-R diagram luminosity axis, the increase in t_* could be a factor of 2–4. Second, this nearer distance would lead to a substantial discrepancy in the ρ Oph and Taurus M_d distributions, such that disks in the former region would be significantly less massive. Taken together, using a distance as close as 125 pc would imply that ρ Oph YSOs are *older* than their Taurus counterparts, and that disk masses have decreased substantially over the corresponding age difference. Obviously using ages from the H-R diagram is not an ideal way to constrain a cluster distance. However, in this case it does not really make sense that the much more deeply embedded YSOs in ρ Oph are older than their essentially unobscured Taurus counterparts. Perhaps this issue can be resolved with a more complete census of the stellar population in the ρ Oph clouds, along the lines of the work done by Wilking et al. (2005) and Doppmann et al. (2003, 2005).

4.3. Benchmark Submillimeter Properties of Circumstellar Disks

Now that large submillimeter photometry samples of YSOs for the ρ Oph and Taurus associations have been collected, it is appropriate to present quantitative reference values for some of the basic properties of their circumstellar environments. The cumulative distributions of the censored datasets presented above were used to determine the median values of M_d , M_d/M_* , and α compiled in Table 4 for various evolutionary states. Here we have distinguished the Class III sources ($n > 1.6$) into two categories: those with submillimeter detections are termed “transition” objects (because dust in the inner disk is largely absent, while a significant outer disk remains) and those undetected sources retain the standard Class III label. These benchmark values clearly highlight the evolution in the submillimeter properties that have been carefully determined in this work and Paper I. Figure 9 graphically illustrates the trend of decreasing $\langle M_d \rangle$ along this sequence, with representative error bars showing the distribution quartiles. Typical disk masses are similar to the MMSN for much of their evolution, only dropping substantially at the end of the Class II stage. The transition disks have a typical disk mass roughly an order of magnitude lower than the MMSN

value, corresponding roughly to a Jupiter mass of material. The stringent stacked upper limit placed on the remaining Class III disks is more than an order of magnitude lower still, suggesting that primordial circumstellar disks at this stage in evolution are probably non-existent. However, this limit still does not rule out the presence of low-mass debris disks similar to those noted around older nearby stars (e.g., Holland et al. 1998).

The accretion disks present in the Class II stage of evolution are generally regarded as the birthsites of planetary systems. As such, their properties are directly relevant for constraining the initial conditions available for the planet formation process. In light of their significance in this matter, Figure 10 shows the differential M_d and α distributions for the ρ Oph and Taurus Class II sources that have firm submillimeter detections. Compiled from 125 individual sources, this distribution of disk masses peaks at $\sim 0.01 M_\odot$ (the MMSN value) and covers a fairly wide dispersion. As would be expected from the analysis of individual regions presented here and in Paper I, the α distribution for these sources has a relatively narrow peak centered around $\alpha \approx 2$. With the similarities between the disk properties in the two star-forming regions (§3.3), these values should represent a combined, universal description of the most basic submillimeter properties of Class II disks.

But how precisely are the values of these properties constrained in an absolute sense? Of course, the submillimeter colors are empirically measured quantities and, aside from occasionally large error bars, their values are firmly determined. The challenge is interpreting the α values in terms of the solid particle population in these disks. The evidence is now fairly clear on the observational side that the typical disk opacity spectrum is more shallow than in the ISM, with $\beta \sim 1$ deemed appropriate to explain the submillimeter SEDs (e.g., Paper I; Beckwith & Sargent 1991; Mannings & Emerson 1994; Rodmann et al. 2006; Andrews & Williams 2007). This effect has been interpreted as the signature of an increase in the maximum dust particle size, from \sim sub-micron sizes in the ISM to \sim millimeter sizes in a typical disk (Miyake & Nakagawa 1993; Pollack et al. 1994; Henning & Stognienko 1996; D’Alessio et al. 2001; Draine 2006). This amounts to ~ 4 orders of magnitude in particle growth from the time when these dust grains were incorporated into circumstellar disks/envelopes from the ISM. Moreover, D’Alessio et al. (2001) emphasize that this actually represents a lower limit on the amount of particle growth, as β remains near unity for maximum particle sizes well beyond the (sub-)millimeter wavelengths used to constrain it (see their Fig. 3). In essence, submillimeter colors indicate that significant grain growth has occurred in these disks, although it remains unclear exactly how far along it may have proceeded beyond millimeter sizes.

In a sense, the opacity acts as an accounting system for the mass budget in a disk. Not all solid particle sizes are generating sufficiently detectable emission at submillimeter wavelengths, and the opacity must also represent the mass contribution of the inefficient emitters in the conversion of a submillimeter luminosity to a disk mass. A direct, non-degenerate measurement of κ_ν in a disk is not currently possible, and so a standard approximate value has been fixed and regularly utilized in this field. In their admittedly simplified analysis, D’Alessio et al. (2001) show that this fixed

opacity value, $\kappa_{1.3\text{mm}} \approx 0.02 \text{ cm}^2 \text{ g}^{-1}$ (as well as $\beta = 1$), is appropriate when the largest particle sizes are $\sim 1 \text{ mm}$. However, the opacity is significantly diminished when the maximum particle size is larger than this value. Because $M_d \propto L_{\text{submm}}/\kappa_\nu$, an underestimate of the amount of particle growth in these disks implies an underestimate of their masses.

Using laboratory experiments and computer models as a guide for the collision conditions in the disk interior, Dominik et al. (2007) argue that solid bodies up to \sim meter size scales can be formed on rather short timescales. The work by D’Alessio et al. (2001) shows that meter-sized bodies would have an opacity $\sim 10\times$ lower than what has been assumed here (but with the same value of β). If such growth is typical, the inferred disk masses may be underestimated by an order of magnitude. Hartmann et al. (1998) proposed an interesting test on the validity of the standard opacity prescription. Aside from the method used here based on the submillimeter continuum emission from dust, they argued that mass accretion rates (\dot{M}) determined from optical/ultraviolet spectra can be used to estimate M_d with some reasonable assumptions about the accretion history. Their disk mass estimates, $M_d \approx 2t_*\dot{M}$, are based solely on observations of the gas phase in the disks, and are therefore completely independent of the values presented here (see Hartmann et al. 1998, regarding the numerical factor of 2). Using the stellar ages derived in the previous section and the accretion rates compiled by Hartmann et al. (1998) and Natta et al. (2006), disk masses were calculated using both methods for the subset of ρ Oph and Taurus Class II sources with the required information available (i.e., \dot{M} , t_* , and a millimeter detection).¹

A comparison of the two methods for computing M_d in Figure 11 clearly demonstrates that disk masses estimated from dust emission are systematically smaller than those inferred from the accretion rates. The dotted line in this plot has a slope of unity and bisects the sample into equal-sized groups: it lies roughly an order of magnitude below the solid line marking equality between the two M_d determination methods. Of course, both methods of estimating M_d involve significant uncertainties. The unknown disk structure in most cases can lead to relatively small uncertainties on the M_d values determined from submillimeter continuum emission (see Paper I; Andrews & Williams 2007). Larger uncertainties plague the M_d estimates from the Hartmann et al. (1998) method, due to both the subtleties of determining \dot{M} and the challenges of specifying individual stellar ages. While these undoubtedly contribute to the scatter in Figure 11, they are unlikely to cause the noted *systematic* offset. For example, a temperature uncertainty could easily translate to a 50% M_d uncertainty (see Eqn. 2) for a given disk. But, the scatter in Figure 2 shows that it is improbable that the average adopted T_c is systematically $2\times$ lower than assumed (let alone the $10\times$ needed to explain Figure 11). A similar argument holds for other disk structure parameters and the stellar ages used in determining M_d from the accretion rate.

Perhaps a variety of uncertainties can unfortunately conspire to produce the observed offset. To be fair, this comparison of M_d estimates from different material phases and spatial locations

¹We preferred to re-calculate the accretion rates provided by Natta et al. (2006) based on the stellar parameters adopted throughout this paper. Regardless, the results in Figure 11 stand irrespective of whose numbers are used.

(gas near the inner rim and dust spread to the outer radius) relies on the assumption that accretion disks can be approximated with relatively simple physical prescriptions. However, given all of these caveats, Figure 11 is really the only check on the absolute precision of M_d measurements currently available. If solely physical explanations are considered to explain these results, the growth of solid particles to centimeter or meter size scales (rather than the millimeter scales that correspond to the standard opacity prescription) is perhaps the most likely cause. Such growth is observationally reinforced by the remarkable centimeter-wave dust emission from large particles recently detected for the TW Hya disk (Wilner et al. 2005).

As discussed above, the decrease in the opacity expected from this level of grain growth corresponds to disk masses being under-estimated by up to an order of magnitude. If this is the case, the implications for the planet formation process are significant. The appropriate shift in the M_d distributions presented here to account for the κ_ν over-estimate could imply that a relatively large fraction (perhaps up to one third) of ~ 1 Myr old Class II disks are massive enough to be gravitationally unstable (i.e., $M_d/M_* \gtrsim 0.2$; Shu et al. 1990). If these instabilities are indeed common, the giant planet formation process may be rapidly accelerated via direct condensations from spiral density waves/rings (e.g., Boss 1998; Mayer et al. 2007), compared to the standard core accretion and gas capture models (e.g., Pollack et al. 1996; Hubickyj et al. 2005). A concerted effort utilizing both high spatial and spectral resolution multiwavelength submillimeter data (e.g., from the ALMA and e-VLA interferometers) and state-of-the-art disk models may help shed some light on this subject in the near future.

5. Summary

We have presented new multiwavelength submillimeter continuum observations of 48 YSOs in the ρ Oph dark clouds. Supplementing this survey with 99 millimeter measurements in the literature, we study the circumstellar dust around young stars in this region; the results are summarized here.

- The statistical distributions of disk masses (M_d), disk-to-star mass ratios, and submillimeter colors (α ; where $F_\nu \propto \nu^\alpha$) were derived and directly compared with those for the Taurus association (Andrews & Williams 2005). Within the uncertainties, there are no significant differences between the submillimeter properties of YSOs in the two regions.
- There are statistically significant decreases in M_d and α along the canonical YSO evolution sequence based on the shape of the infrared SED. Changes in the structure of the circumstellar environment and/or the average particle properties may explain the correlations.
- A tentative correlation between the disk-to-star mass ratio and stellar age are noted for the combined samples in both regions. Confirmation with older sources would be beneficial to assess whether or not this relationship depends on isochrone models at early ages ($\sim 10^5$ yr).

- The Class II YSOs in ρ Oph and Taurus are utilized to establish benchmark values for sub-millimeter properties in the population considered to be the birthsites of planetary systems: $M_d \sim 0.005 M_\odot$, $M_d/M_* \sim 1\%$, and $\alpha \sim 2$.
- An independent disk mass estimate based on the accretion rate (Hartmann et al. 1998) is used to compare with the submillimeter continuum measurements. The latter are systematically smaller than the former by roughly an order of magnitude on average. This may be the result of substantial particle growth (up to \sim meter sizes), leading to an over-estimate of the opacity used to compute M_d from the submillimeter luminosity. Such disk mass underestimates may imply that some fraction of Class II disks are marginally gravitationally unstable, which could have important implications for disk evolution and giant planet formation.

We acknowledge useful conversations and advice from Lee Hartmann, Eric Mamajek, and an anonymous referee. We would especially like to thank Lori Allen, Rob Gutermuth, and their colleagues for providing very useful *Spitzer* data before publication, as well as the JCMT and CSO support staffs for their assistance. This work was supported by the NASA Graduate Student Researchers Program (GSRP) grant NNG05G012H and the NSF grant AST-0324328. This research has made use of the NASA/IPAC Infrared Science Archive, which is operated by the Jet Propulsion Laboratory, California Institute of Technology, under contract with the National Aeronautics and Space Administration.

REFERENCES

- Adams, F. C., & Shu, F. H. 1986, *ApJ*, 308, 836
- Adams, F. C., Lada, C. J., & Shu, F. H. 1987, *ApJ*, 312, 788
- Alexander, R. D., Clarke, C. J., & Pringle, J. E. 2006, *MNRAS*, 369, 229
- Allen, L. E., 2007, private communication
- André, P., Montmerle, T., Feigelson, E. D., & Steppe, H. 1990, *A&A*, 240, 321
- André, P., & Montmerle, T. 1994, *ApJ*, 420, 837
- Andrews, S. M., & Williams, J. P. 2005, *ApJ*, 635, 1134 (Paper I)
- Andrews, S. M., & Williams, J. P. 2007, *ApJ*, 695, 734
- Barsony, M., Ressler, M. E., & Marsh, K. A. 2005, *ApJ*, 630, 381
- Beckwith, S. V. W., Sargent, A. I., Chini, R. S., & Güsten, R. 1990, *AJ*, 99, 924
- Beckwith, S. V. W., & Sargent, A. I. 1991, *ApJ*, 381, 250

- Bontemps, S., et al. 2001, *A&A*, 372, 173
- Boss, A. P. 1998, *ApJ*, 503, 923
- Bouvier, J., & Appenzeller, I. 1992, *A&AS*, 92, 481
- Brandner, W., & Zinnecker, H. 1997, *A&A*, 321, 220
- Carpenter, J. M. 2002, *AJ*, 124, 1593
- Chavarría, K. C., Terranegra, L., Moreno-Corral, M. A., & de Lara, E. 2000, *A&AS*, 145, 187
- Chiang, E. I., & Goldreich, P. 1997, *ApJ*, 490, 368
- Chini, R. 1981, *A&A*, 99, 346
- Clarke, C. J., Gendrin, A., & Sotomayor, M. 2001, *MNRAS*, 328, 485
- Cohen, J. G., Persson, S. E., Elias, J. H., & Frogel, J. A. 1981, *ApJ*, 249, 481
- Cutri, R. M., et al. 2003
- D'Alessio, P., Cantó, J., Calvet, N., & Lizano, S. 1998, *ApJ*, 500, 411
- D'Alessio, P., Calvet, N., & Hartmann, L. 2001, *ApJ*, 553, 321
- D'Alessio, P., Calvet, N., Hartmann, L., Franco-Hernández, R., & Servín, H. 2006, *ApJ*, 638, 314
- D'Antona, F., & Mazzitelli, I. 1997, in *Cool Stars in Clusters and Associations*, eds. G. Micela & R. Pallavicini (Firenze: Soc. Astron. Italiana), 807
- de Geus, E. J., de Zeeuw, P. T., & Lub, J. 1989, *A&A*, 216, 44
- de Geus, E. J., & Burton, W. B. 1991, *A&A*, 246, 559
- de Zeeuw, P. T., Hoogerwerf, R., de Bruijne, J. H. J., Brown, A. G. A., & Blaauw, A. 1999, *AJ*, 117, 354
- Dominik, C., Blum, J., Cuzzi, J. N., & Wurm, G. 2007, in *Protostars and Planets V*, eds. B. Reipurth, D. Jewitt, & K. Keil (Tucson: Univ. Arizona Press), 783
- Doppmann, G. W., Jaffe, D. T., & White, R. J. 2003, *AJ*, 126, 3043
- Doppmann, G. W., Greene, T. P., Covey, K. R., & Lada, C. J. 2005, *AJ*, 130, 1145
- Dowell, C. D. et al. 2003, *Proc. SPIE*, 4855, 73
- Draine, B. T. 2006, *ApJ*, 636, 1114
- Dullemond, C. P., van Zadelhoff, G. J., & Natta, A. 2002, *A&A*, 389, 464

- Dullemond, C. P.
- Eisner, J. A., Hillenbrand, L. A., White, R. J., Akeson, R. L., & Sargent, A. I. 2005, *ApJ*, 623, 952
- Feigelson, E. D., & Nelson, P. I. 1985, *ApJ*, 293, 192
- Gomez, M., Hartmann, L., Kenyon, S. J., & Hewett, R. 1993, *AJ*, 105, 1927
- Grankin, K. N., Melnikov, S. Y., Bouvier, J., Herbst, W., & Shevchenko, V. S. 2007, *A&A*, 461, 183
- Gras-Velázquez, À., & Ray, T. P. 2005, *A&A*, 443, 541
- Greene, T. P., & Young, E. T. 1992, *ApJ*, 395, 516
- Greene, T. P., Wilking, B. A., André, P., Young, E. T., & Lada, C. J. 1994, *ApJ*, 434, 614
- Greene, T. P., & Meyer, M. R. 1995, *ApJ*, 450, 233
- Hartmann, L., Calvet, N., Gullbring, E., & D'Alessio, P. 1998, *ApJ*, 495, 385
- Hartmann, L., et al. 2005, *ApJ*, 629, 881
- Henning, T., & Stognienko, R. 1996, *A&A*, 311, 291
- Herbig, G. H., & Bell, K. R. 1988, *Lick Obs. Bull.*, 1111, 1
- Herbst, W., Herbst, D. K., Grossman, E. J., & Weinstein, D. 1994, *AJ*, 108, 1906
- Hildebrand, R. 1983, *QJRAS*, 24, 267
- Holland, W. S. et al. 1998, *Nature*, 392, 788
- Holland, W. S. et al. 1999, *MNRAS*, 303, 659
- Hubickyj, O., Bodenheimer, P., & Lissauer, J. J. 2005, *Icarus*, 179, 415
- Isobe, T., Feigelson, E. D., & Nelson, P. I. 1986, *ApJ*, 306, 490
- Jensen, E. L. N., Mathieu, R. D., & Fuller, G. A. 1996, *ApJ*, 458, 312
- Kenyon, S. J., & Hartmann, L. 1995, *ApJS*, 101, 117
- Kitamura, Y., Momose, M., Yokogawa, S., Kawabe, R., Tamura, M., & Ida, S. 2002, *ApJ*, 581, 357
- Knude, J., & Høg, E. 1998, *A&A*, 338, 897
- Lada, C. J., & Wilking, B. A. 1984, *ApJ*, 287, 610
- Li, A., & Draine, B. T. 2001, *ApJ*, 554, 778

- Lissauer, J. J., & Stevenson, D. J. 2007, in *Protostars and Planets V*, eds. B. Reipurth, D. Jewitt, & K. Keil (Tucson: Univ. Arizona Press), 591
- Lommen, D., et al. 2007, *A&A*, 462, L211
- Luhman, K. L., & Rieke, G. H. 1999, *ApJ*, 525, 440
- Luhman, K. L., Whitney, B. A., Meade, M. R., Babler, B. L., Indebetouw, R., Bracker, S., & Churchwell, E. B. 2006, *ApJ*, 647, 1180
- Lynden-Bell, D., & Pringle, J. E. 1974, *MNRAS*, 168, 603
- Mamajek, E. E. 2007, *Astronomische Nachrichten*, in press
- Mannings, V., & Emerson, J. P. 1994, *MNRAS*, 267, 361
- Mayer, L., Lufkin, G., Quinn, T., & Wadsley, J. 2007, *ApJ*, 661, L77
- Miyake, K., & Nakagawa, Y. K. 1993, *Icarus*, 106, 20
- Motte, F., André, P., & Neri, R. 1998, *A&A*, 336, 150
- Myers, P. C., Fuller, G. A., Mathieu, R. D., Beichman, C. A., Benson, P. J., Schild, R. E., & Emerson, J. P. 1987, *ApJ*, 319, 340
- Najita, J. R., Strom, S. E., & Muzerolle, J. 2007, *MNRAS*, 378, 369
- Natta, A., Testi, L., & Randich, S. 2006, *A&A*, 452, 245
- Natta, A., Testi, L., Calvet, N., Henning, T., Waters, R., & Wilner, D. 2007, in *Protostars and Planets V*, eds. B. Reipurth, D. C. Jewitt, & K. Keil (Tucson: Univ. Arizona Press), 767
- Nürnbergger, D., Brandner, W., Yorke, H. W., & Zinnecker, H. 1998, *A&A*, 330, 549
- Osterloh, M., & Beckwith, S. V. W. 1995, *ApJ*, 439, 288
- Padgett, D. L., et al. 2006, *ApJ*, 645, 1283
- Pollack, J. B., Hollenbach, D., Beckwith, S., Simonelli, D. P., Roush, T., & Fong, W. 1994, *ApJ*, 4241, 615
- Pollack, J. B., Hubickyj, O., Bodenheimer, P., Lissauer, J. J., Podolak, M., & Greenzweig, Y. 1996, *Icarus*, 124, 62
- Prato, L., Greene, T. P., & Simon, M. 2003, *ApJ*, 584, 853
- Rodmann, J., Henning, T., Chandler, C. J., Mundy, L. G., & Wilner, D. J. 2006, *A&A*, 446, 211
- Rydgren, A. E. 1980, *AJ*, 85, 438

- Shu, F. H., Tremaine, S., Adams, F. C., & Ruden, S. P. 1990, *ApJ*, 358, 495
- Stanke, T., Smith, M. D., Gredel, R., & Khanzadyan, T. 2006, *A&A*, 447, 609
- Terebey, S., Shu, F. H., & Cassen, P. 1984, *ApJ*, 286, 529
- Testi, L., Natta, A., Shepherd, D. S., & Wilner, D. J. 2001, *ApJ*, 554, 1087
- Testi, L., Natta, A., Shepherd, D. S., & Wilner, D. J. 2003, *A&A*, 403, 323
- Vrba, F. J., Coyne, G. V., & Tapia, S. 1993, *AJ*, 105, 1010
- Weaver, W. B., & Jones, G. 1992, *ApJS*, 78, 239
- Weidenschilling, S. J. 1977, *Ap&SS*, 51, 153
- Whittet, D. C. B. 1974, *MNRAS*, 168, 371
- Wilking, B. A., Lada, C. J., & Young, E. T. 1989, *ApJ*, 340, 823
- Wilking, B. A., Greene, T. P., & Meyer, M. R. 1999, *AJ*, 117, 469
- Wilking, B. A., Meyer, M. R., Robinson, J. G., & Greene, T. P. 2005, *AJ*, 130, 1733
- Wilner, D. J., D’Alessio, P., Calvet, N., Claussen, M. J., & Hartmann, L. 2005, *ApJ*, 626, 109

Table 1. Submillimeter Properties of Circumstellar Disks in ρ Ophiuchus

Object (1)	SED (2)	SpT (3)	$F_\nu(350\ \mu\text{m})$ [mJy] (4)	$F_\nu(450\ \mu\text{m})$ [mJy] (5)	$F_\nu(850\ \mu\text{m})$ [mJy] (6)	$F_\nu(1.3\ \text{mm})$ [mJy] (7)	M_d [M_\odot] (8)	α (9)	Notes (10)
Wa Oph 1, HBC 630	III	K2	...	< 114	< 8	< 20	< 0.0005	...	1
AS 205, HBC 254	II	K5	4683 ± 118	3280 ± 271	891 ± 11	450 ± 10	0.03	1.85 ± 0.21	1
Wa Oph 2, HBC 633	III	K1	...	< 129	< 9	< 20	< 0.0006	...	1
Wa Oph 3, HBC 634	III	K0	...	< 145	< 10	< 25	< 0.0006	...	1
WSB 3	III	M3	< 34	...	< 0.002	...	2
WSB 4	III	M3	< 13	< 0.003	...	3
WSB 11	II	< 26	...	< 0.001	...	2
L1719 B, 16191-1936	FS	220 ± 10	0.04	...	1
WSB 18	III	M2	< 46	...	< 0.003	...	2
WSB 19	II	M3	< 78	...	< 0.004	...	2
DoAr 16, HBC 257	II	K6	...	< 361	47 ± 8	< 50	0.003	< 3.21	1
SR 1, EL 9, GSS 9	III	B2	...	< 154	< 11	< 50	< 0.0007	...	1
SR 22, DoAr 19	II	M4	...	< 162	31 ± 3	< 20	0.002	< 2.60	1
ROXs 2, VSS 20	III	M0	...	< 156	< 11	< 30	< 0.0007	...	1
IRS 2, YLW 19	II	K3	< 25	< 0.005	...	1
IRS 7	II	< 40	< 0.008	...	1
IRS 8	III	< 40	< 0.008	...	1
IRS 9, YLW 23	III	< 10	< 0.002	...	1
ROXs 3, HBC 636	III	M0	< 30	< 0.006	...	1
IRS 10, ROXs 4	III	K6	< 28	< 0.005	...	3
ROXs 5	III	K7	< 19	< 0.004	...	3
SR 4, AS 206	II	K5	...	< 768	142 ± 7	31 ± 6	0.004	1.50 ± 0.62	3
IRS 13, ROXs 7	III	K6	< 20	< 0.004	...	1
DoAr 21, HBC 637	III	K1	< 30	< 0.006	...	4
SR 3, IRS 16	III	A0	< 25	< 0.005	...	1
GSS 26	II	K8	...	650 ± 123	298 ± 7	125 ± 20	0.04	1.65 ± 0.36	4
EL 18, GSS 29	II	K6	< 10	< 0.002	...	4
DoAr 24, HBC 638	II	K5	< 30	< 0.006	...	4
CRBR 12, ISO-Oph 21	I	85 ± 5	0.02	...	4
DoAr 23, WSB 26	III	M0	< 77	...	< 0.004	...	2
EL 20, VSSG 1	II	< 666	240 ± 7	50 ± 10	0.03	3.69 ± 0.71	1
CRBR 15	I	M5	40 ± 5	0.008	...	4
EL 21, GSS 30	I	1403 ± 116	222 ± 5	90 ± 30	0.01	2.50 ± 0.33	4
LFAM 1	FS	2662 ± 219	572 ± 8	250 ± 20	0.04	2.18 ± 0.31	4
GY 10	III	M9	< 10	< 0.002	...	4
GY 11	FS	M7	< 10	< 0.002	...	4
DoAr 24E, GSS 31	II	K1	...	779 ± 121	158 ± 6	70 ± 20	0.008	2.32 ± 0.43	4
DoAr 25, WSB 29	II	K5	461 ± 11	280 ± 10	0.03	1.17 ± 0.54	1
LFAM 3, GY 21	FS	110 ± 10	0.02	...	4
ROXs 9A	III	M0	< 22	< 0.004	...	3
EL 24, WSB 31	II	K6	5242 ± 213	3012 ± 216	838 ± 8	390 ± 10	0.2	1.99 ± 0.22	1
ROXs 12	III	M0	< 19	< 0.004	...	3
VSSG 27, GY 51	II	< 20	< 0.004	...	4
ROXs 9B	III	K2	< 11	< 0.002	...	3

Table 1—Continued

Object (1)	SED (2)	SpT (3)	$F_\nu(350\ \mu\text{m})$ [mJy] (4)	$F_\nu(450\ \mu\text{m})$ [mJy] (5)	$F_\nu(850\ \mu\text{m})$ [mJy] (6)	$F_\nu(1.3\ \text{mm})$ [mJy] (7)	M_d [M_\odot] (8)	α (9)	Notes (10)
IRS 14, GY 54	II	< 30	< 0.006	...	1
IRS 15, GY 58	II	< 30	< 0.006	...	1
S1, EL 25, GSS 35	III	B3	< 10	< 0.002	...	4
ROXs 9C	III	K4	< 14	< 0.003	...	3
GY 91	I	300 ± 15	0.06	...	4
WSB 37, GY 93	II	M5	< 25	< 0.005	...	1
WL 8, GY 96	II	< 10	< 0.002	...	4
IRS 17, WL 7	FS	< 30	< 0.006	...	4
ROC 16, GY 101	FS	< 15	< 0.003	...	4
EL 26, GSS 37	II	M0	< 51	15 ± 5	0.005	< 2.88	1
IRS 19, VSSG 11	III	M0	< 15	< 0.003	...	1
WL 12, YLW 2	I	749 ± 130	216 ± 7	115 ± 10	0.01	2.00 ± 0.36	4
EL 27, GSS 39	II	K8	...	2737 ± 322	678 ± 10	300 ± 10	0.04	2.07 ± 0.32	1
ROXs 9D	III	< 35	< 0.007	...	3
WSB 38, VSS 27	III	G4	< 20	< 0.004	...	1
DoAr 28, HBC 261	II	K5	< 75	< 0.01	...	1
WL 2, GY 128	FS	30 ± 10	0.006	...	4
WL 18, GY 129	II	K7	85 ± 10	0.02	...	4
IRS 23, WL 21	III	< 30	< 0.006	...	4
CRBR 51	FS	70 ± 15	0.01	...	4
SR 24, HBC 262	FS	K1	1271 ± 32	1263 ± 282	530 ± 9	230 ± 11	0.03	1.29 ± 0.23	3
WL 14, GY 172	II	M4	30 ± 10	0.006	...	4
IRS 27, WL 22	I	< 438	70 ± 5	40 ± 10	0.004	1.99 ± 0.96	4
WL 16, YLW 5	FS	< 6	< 0.001	...	4
IRS 29, WL 1	FS	< 702	15 ± 4	< 20	0.0009	< 6.05	4
LFAM 26, GY 197	I	100 ± 10	0.02	...	4
WL 17, GY 205	I	< 867	100 ± 7	75 ± 10	0.006	0.84 ± 0.65	4
WL 10, GY 211	II	K8	< 60	< 0.01	...	4
GY 213	II	40 ± 10	0.008	...	4
EL 29, WL 15	I	2024 ± 109	408 ± 6	95 ± 10	0.03	2.82 ± 0.32	4
SR 21, EL 30	II	G3	2761 ± 57	1896 ± 268	397 ± 6	95 ± 15	0.03	2.27 ± 0.22	4
IRS 31, WL 9	II	< 10	< 0.002	...	4
GY 224	I	50 ± 10	0.01	...	4
WL 19, GY 227	II	30 ± 10	0.006	...	4
WL 11, GY 229	II	< 10	< 0.002	...	4
WSB 45, HBC 640	III	M5	< 20	< 0.004	...	1
IRS 33, GY 236	II	105 ± 20	0.02	...	4
WSB 46, HBC 641	II	M2	< 20	< 0.004	...	1
IRS 34, GY 239	II	< 20	< 0.004	...	4
IRS 36, GY 241	FS	< 15	< 0.003	...	4
WL 20, GY 240	I	400 ± 112	182 ± 6	47 ± 1	0.01	1.39 ± 0.40	5
IRS 37, GY 244	II	M4	...	< 591	93 ± 8	< 10	0.006	1.03 ± 0.69	4
IRS 38, WL 5	III	F7	...	< 522	80 ± 4	< 10	0.005	< 4.89	4
GY 245	FS	60 ± 5	0.01	...	4

Table 1—Continued

Object (1)	SED (2)	SpT (3)	$F_\nu(350\ \mu\text{m})$ [mJy] (4)	$F_\nu(450\ \mu\text{m})$ [mJy] (5)	$F_\nu(850\ \mu\text{m})$ [mJy] (6)	$F_\nu(1.3\ \text{mm})$ [mJy] (7)	M_d [M_\odot] (8)	α (9)	Notes (10)
IRS 39, WL 4	II	M2	...	< 480	63 ± 5	< 15	0.01	1.75 ± 0.96	4
IRS 41, WL 3	II	< 582	115 ± 4	< 60	0.007	< 2.55	4
SR 12, HBC 263	III	M0	< 26	< 20	< 0.001	...	2,4
IRS 42, GY 252	II	< 60	< 0.01	...	4
WL 6, GY 254	FS	< 20	< 0.004	...	4
VSSG 22, ROXs 23	III	K6	< 30	< 0.006	...	1
WSB 49	II	M4	< 25	< 0.005	...	1
CRBR 85	II	150 ± 10	0.03	...	4
YLW 16C, GY 262	II	M1	60 ± 5	0.03	...	4
IRS 43, YLW 15	I	1811 ± 358	246 ± 7	80 ± 10	0.02	2.99 ± 0.38	4
EL 31, WL 13	II	M0	< 10	< 0.002	...	4
IRS 44, GY 269	I	60 ± 10	0.01	...	4
EL 32, IRS 45	II	K7	< 50	< 0.01	...	4
IRS 46, GY 274	FS	45 ± 10	0.009	...	4
EL 33, IRS 47	II	< 20	< 0.004	...	4
GY 284	II	M3	130 ± 10	0.02	...	4
ROXs 25, GY 292	II	M2	30 ± 5	0.007	...	4
ROXs 30A	III	< 10	< 0.002	...	3
IRS 48, GY 304	I	< 1566	180 ± 9	60 ± 10	0.01	1.91 ± 0.61	4
IRS 50, GY 306	III	M4	< 10	< 0.002	...	4
IRS 49, GY 308	II	K8	...	< 1041	52 ± 5	25 ± 5	0.003	1.71 ± 1.10	1
DoAr 32, WSB 51	II	K6	< 45	< 0.009	...	1
DoAr 33, WSB 53	II	K4	...	< 678	79 ± 7	40 ± 10	0.005	1.60 ± 0.82	1
WSB 52, GY 314	II	K5	51 ± 10	0.007	...	6
IRS 51, GY 315	II	< 678	171 ± 6	110 ± 10	0.01	< 2.17	4
SR 9, AS 207	II	K5	< 25	15 ± 5	0.002	< 1.20	1
EL 36, VSSG 14	II	A7	< 10	< 0.002	...	3
IRS 54, GY 378	FS	30 ± 10	0.006	...	4
ROXs 31, HBC 642	III	K8	< 22	< 25	< 0.001	...	1,2
SR 10, HBC 265	II	M2	< 25	< 0.005	...	1
WSB 60, YLW 58	II	M4	832 ± 67	651 ± 161	149 ± 7	89 ± 2	0.03	1.59 ± 0.24	5
SR 20, HBC 643	III	G7	< 25	< 35	< 0.002	...	1
SR 13, HBC 266	II	M4	...	740 ± 200	118 ± 6	60 ± 10	0.01	2.30 ± 0.42	1
WSB 63	II	M2	< 25	< 0.005	...	1
ROXs 35A	III	K3	< 29	< 0.006	...	3
VSS 44, ROXs 35B	III	G5	< 19	< 0.004	...	3
ROXs 39	III	K6	< 30	< 0.006	...	1
DoAr 42, HBC 267	III	M0	< 30	< 0.006	...	1
ROXs 42B	III	M0	< 45	< 0.009	...	1
ROXs 42C	II	K6	< 30	< 0.006	...	1
ROXs 43A	II	G0	< 35	< 0.007	...	1
ROXs 43B	III	K5	< 17	< 0.003	...	3
IRS 60	II	< 50	< 0.01	...	1
DoAr 44, HBC 268	II	K3	...	< 414	181 ± 6	105 ± 11	0.01	1.28 ± 0.59	3

Table 1—Continued

Object (1)	SED (2)	SpT (3)	$F_\nu(350\ \mu\text{m})$ [mJy] (4)	$F_\nu(450\ \mu\text{m})$ [mJy] (5)	$F_\nu(850\ \mu\text{m})$ [mJy] (6)	$F_\nu(1.3\ \text{mm})$ [mJy] (7)	M_d [M_\odot] (8)	α (9)	Notes (10)
IRS 63, L1709 B	I	...	6703 ± 162	4729 ± 199	1017 ± 7	370 ± 10	0.06	2.28 ± 0.33	1
ROXs 45B	III	< 19	< 0.004	...	3
ROXs 45C	III	K5	< 19	< 0.004	...	3
ROXs 45D	III	K0	< 19	< 0.004	...	3
IRS 67, L1689 S	I	1687 ± 207	394 ± 9	150 ± 10	0.02	2.28 ± 0.33	1
DoAr 51, HBC 647	III	M0	< 20	< 0.004	...	1
IRS 69	II	< 75	< 0.01	...	1
DoAr 52, HBC 648	II	M2	< 55	< 0.01	...	1
RNO 90, HBC 649	II	G5	...	557 ± 83	162 ± 4	25 ± 5	0.005	2.40 ± 0.43	1
RNO 91, HBC 650	FS	M1	...	1524 ± 87	365 ± 9	90 ± 10	0.02	2.64 ± 0.32	1
EL 49	II	58 ± 5	0.01	...	3
Wa Oph 4, HBC 652	II	K4	< 13	< 0.003	...	1
Wa Oph 6, HBC 653	II	K6	...	979 ± 297	379 ± 7	130 ± 10	0.08	2.07 ± 0.40	1
Wa Oph 5, HBC 654	II	M2	< 25	< 0.005	...	1
AS 209, HBC 270	II	K5	3000 ± 72	1915 ± 206	551 ± 10	300 ± 10	0.05	1.80 ± 0.22	1

Note. — Col. (1): Object name(s). Col. (2): SED classification type (FS = Flat Spectrum); see §3.3 for details. Col. (3): Stellar spectral type from the literature (see §4.2). Col. (4): $350\ \mu\text{m}$ flux density. Col. (5): $450\ \mu\text{m}$ flux density. Col. (6): $850\ \mu\text{m}$ flux density. Col. (7): $1.3\ \text{mm}$ flux density. Col. (8): Disk mass (see §3.1). Col. (9): Submillimeter continuum slope (see §3.2). Col. (10): Notes on individual sources as follows: (1) The $1.3\ \text{mm}$ flux densities are from André & Montmerle (1994). The $1\ \sigma$ rms uncertainties were typically assumed to be $\sim 10\ \text{mJy}$. (2) $800\ \mu\text{m}$ flux densities from Jensen et al. (1996) are listed in Col. (6). (3) The $1.3\ \text{mm}$ flux densities are from Nürnberger et al. (1998). (4) The $1.3\ \text{mm}$ flux densities are from Motte et al. (1998). (5) The $1.3\ \text{mm}$ flux densities for WL 20 (S) and WSB 60 are from the interferometric survey of Andrews & Williams (2007). (6) The $1.3\ \text{mm}$ flux densities are from Stanke et al. (2006). All flux densities are measured in units of mJy. Upper limits are taken at the $3\ \sigma$ confidence level. Quoted errors are the $1\ \sigma$ rms noise levels and do not include systematic errors in the absolute flux calibration ($\sim 25\%$ at 350 and $450\ \mu\text{m}$, $\sim 10\%$ at $850\ \mu\text{m}$, and $\sim 20\%$ at $1.3\ \text{mm}$).

Table 2. Results of SED Fits

Object (1)	T_1 [K] (2)	q (3)	M_d [$10^{-3} M_\odot$] (4)	$\bar{\chi}^2$ (5)	dof (6)	Notes (7)	Object (1)	T_1 [K] (2)	q (3)	M_d [$10^{-3} M_\odot$] (4)	$\bar{\chi}^2$ (5)	dof (6)	Notes (7)
AS 205	304	0.55	33 ± 5	2.6	7	1,2,3	IRS 49	142	0.58	2.9 ± 0.6	0.5	3	1,2,5
SR 4	181	0.47	3.8 ± 0.5	0.6	4	1,2,4	WSB 52	162	0.52	7 ± 3	0.1	3	1,2,5,7
GSS 26	157	0.63	45 ± 11	3.8	4	1,2,4	SR 9	150	0.56	1.9 ± 0.9	8.7	2	1,2,5
EL 20	157	0.69	33 ± 9	3.0	3	1,2,5	WSB 60	99	0.57	32 ± 8	4.0	6	1,2,6
DoAr 24E	218	0.63	8 ± 1	0.3	5	1,2,5,6	SR 13	189	0.63	14 ± 3	1.0	6	1,2,3
EL 24	229	0.65	162 ± 62	1.5	8	1,3,5,6	DoAr 44	169	0.54	10 ± 2	1.2	3	1,2,3
EL 26	116	0.70	5 ± 3	2.2	2	1,2,5	RNO 90	215	0.59	4.7 ± 0.7	5.7	5	1,2,3
IRS 39	104	0.69	14 ± 5	2.0	4	1,2,3,6	Wa Oph 6	157	0.65	81 ± 23	1.5	5	3,8
YLW 16C	120	0.63	26 ± 10	0.2	2	1,2,5	AS 209	230	0.63	52 ± 15	1.0	4	3
GY 292	143	0.63	7 ± 3	2.3	2	1,2,6							

Note. — Col. (1): Object name. Col. (2): Best-fit value of the temperature at 1 AU in K (typical errors are \pm a few K). Col. (3): Best-fit value of the radial power-law index of the temperature profile (typical errors are ± 0.02). Col. (4): Best-fit value and uncertainty of the disk mass. Col. (5): Reduced χ^2 statistic. Col. (6): Number of degrees of freedom in the fit (i.e., number of data points minus number of fitted parameters[=3]). Col. (7): Notes on literature sources for the SED data as follows: (1) *Spitzer* Space Telescope IRAC flux densities (3.6, 4.5, 5.8, 8 μm) from L. Allen (2007, private communication). (2) *Spitzer* Space Telescope MIPS flux density (24 μm) from L. Allen (2007, private communication). (3) *IRAS* flux densities (12, 25, 60 μm) from Weaver & Jones (1992). (4) Mid-infrared photometry (10, 20 μm) from Wilking et al. (1989). (5) Mid-infrared photometry (10, 12 μm) from Barsony et al. (2005). (6) *ISO* photometry (6.7 and 14.3 μm) from Bontemps et al. (2001). (7) Mid-infrared photometry (10, 20 μm) from Greene et al. (1994). (8) *Spitzer* IRAC and MIPS photometry from Padgett et al. (2006).

Table 3. Statistical Comparison of ρ Oph and Taurus Submillimeter Properties

Samples	$P(M_d)$ [%]	$P(\alpha)$ [%]
<i>Regional Comparison</i>		
Tau vs. Oph (all)	35 – 47	9 – 62
Tau I vs. Oph I	20 – 72	54 – 55
Tau II vs. Oph II	7 – 10	3 – 65
Tau III vs. Oph III	9 – 34	...
<i>Evolutionary Comparison</i>		
Oph I vs. Oph II	≥ 99.75	92 – 95
Oph II vs. Oph III	≥ 99.9999	...
Tau I vs. Tau II	≥ 99.97	≥ 99.91
Tau II vs. Tau III	≥ 99.9999	...

Note. — Results of survival analysis two-sample statistical tests comparing various subsamples of the submillimeter properties of Taurus (Paper I) and ρ Oph YSOs. The listed values P correspond to the probabilities that the two subsamples are drawn from *different* parent distributions. The probability ranges are from different statistical tests.

Table 4. Median Submillimeter Properties of YSOs

Sample	$\langle M_d \rangle$ [M_\odot]	$\langle M_d/M_* \rangle$ [%]	$\langle \alpha \rangle$
Class I	0.015	3.8	2.3
Class II	0.005	0.9	1.9
transition ^a	0.0009	0.3	...
Class III	$< 5 \times 10^{-5}$

^aTransition objects are defined here to be Class III sources (i.e., $n > 1.6$) that have submillimeter detections. There is 1 such object in ρ Oph (WL 5) and 7 others in Taurus (CIDA-8, CoKu Tau/4, FW Tau, FY Tau, HQ Tau, LkH α 332/G1, and V807 Tau). The submillimeter detection of WL 5 may be anomalous: Motte et al. (1998) showed that the original quoted 1.3 mm detection from earlier work (André & Montmerle 1994) was actually background emission. The Class III sample median M_d is based on the stacked average limit derived in §4.1.

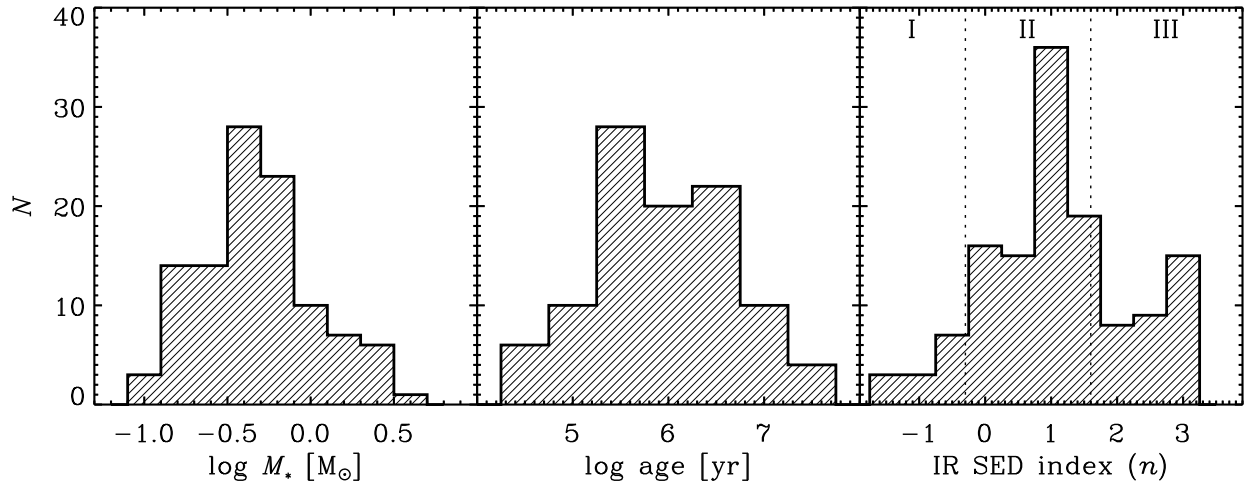


Fig. 1.— Histograms of some relevant properties for the ρ Oph sample objects. The left and middle panels show stellar masses and ages, inferred as described in §4.2 using the D’Antona & Mazzitelli (1997) theoretical pre-main–sequence evolution models. The right panel shows the infrared SED index (defined as n where $\nu F_\nu \propto \nu^n$; see §3.3) that is commonly used as an evolutionary diagnostic for circumstellar dust. YSOs with an index less than -0.3 are Class I sources, between -0.3 and 1.6 are Class II sources, and >1.6 are Class III sources (SED classification borders are shown as dotted vertical lines; Greene et al. 1994).

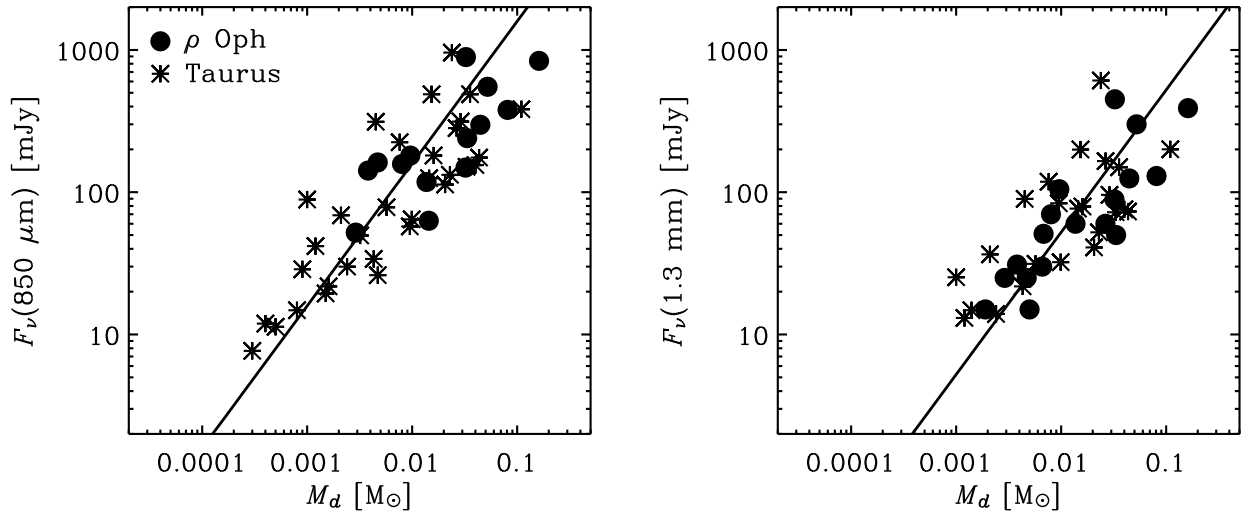


Fig. 2.— Correlations between the $850 \mu\text{m}$ (*left*) or 1.3 mm (*right*) flux densities and the best-fit disk masses inferred from fitting SEDs with a simple disk structure model. The results for ρ Oph (*circles*: see Table 2) and Taurus (*asterisks*: see Paper I) YSOs are shown together (the latter flux densities have been scaled to $d = 150 \text{ pc}$ for ease of comparison). Overlaid as a solid line in each panel is the generic relationship described by Eqn. 2 for $T_c = 20 \text{ K}$, used to calculate disk masses (or upper limits) for the remainder of the sample.

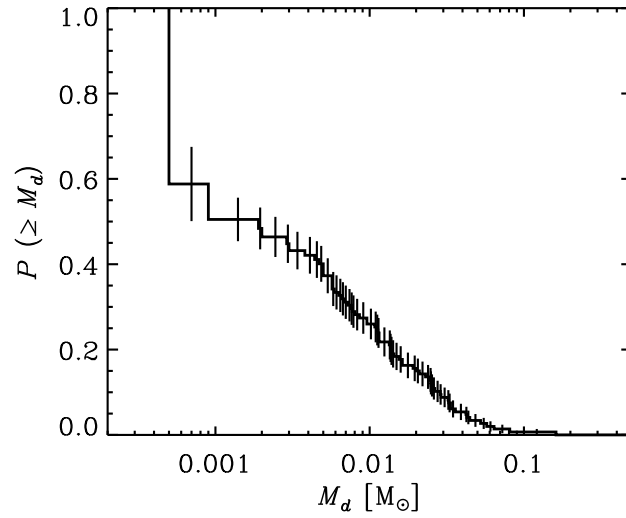


Fig. 3.— The cumulative distribution of disk masses for the ρ Oph sources listed in Table 1, constructed using the Kaplan-Meier estimator to include non-detections. The ordinate represents the probability that a sample disk has a mass greater than the abscissa value. The median disk mass for the full sample is $\sim 0.002 M_\odot$.

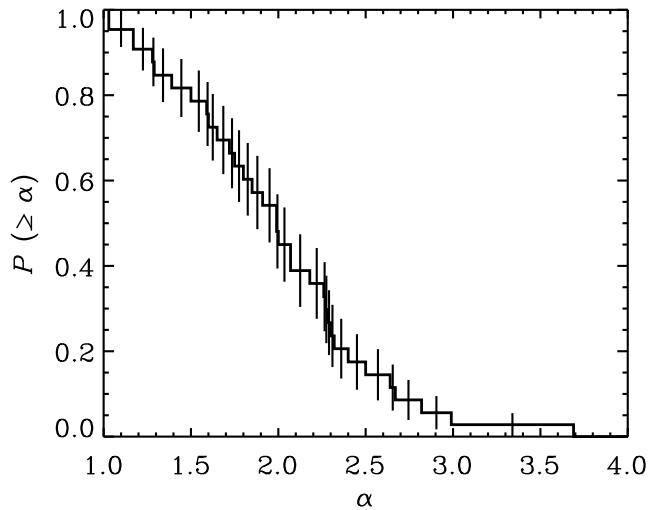


Fig. 4.— The cumulative distribution of submillimeter colors (α , defined as $F_\nu \propto \nu^\alpha$) for the ρ Oph sources listed in Table 1, constructed using the Kaplan-Meier estimator to include non-detections. The ordinate represents the probability that a sample disk has a spectral index greater than the abscissa value. The median value for the full sample is $\langle \alpha \rangle \approx 2.0$.

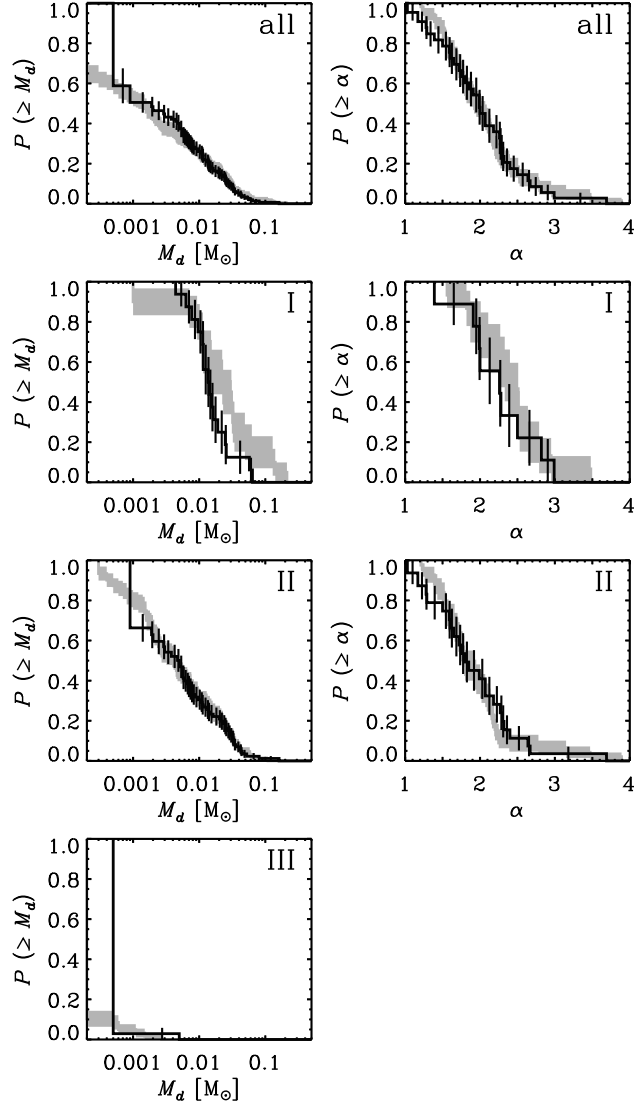


Fig. 5.— Direct comparisons of submillimeter properties in the ρ Oph (black lines) and Taurus (grayscale) regions. The panels on the left and right show the cumulative distributions of M_d and α , respectively, for various subgroups of YSOs in each region. The top panels show the full samples described here and in Paper I. The subsequent panels below show the distributions for Class I, II, and III sources. The distributions of these submillimeter properties in the ρ Oph and Taurus regions are essentially indistinguishable. However, there are statistically significant changes in the M_d and α distributions along the Class I \rightarrow II \rightarrow III evolution sequence.

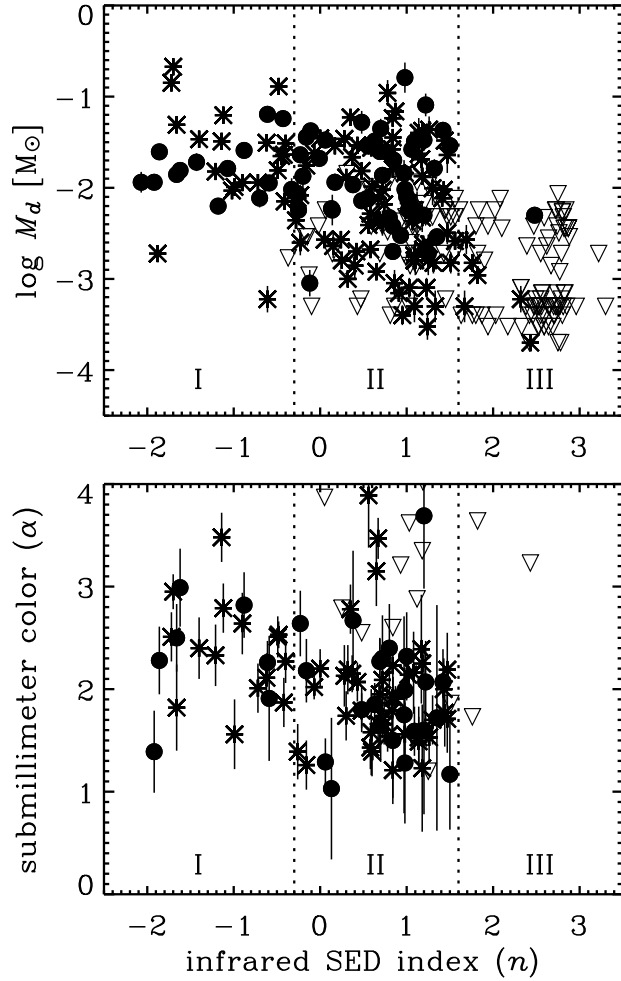


Fig. 6.— Individual disk masses (*top*) and submillimeter colors (α : *bottom*) as a function of the infrared SED index measured between $\sim 2\text{--}25\ \mu\text{m}$ (n) for the combined ρ Oph (*circles*) and Taurus (*asterisks*) samples. Open triangles represent upper limits. Both panels show correlations such that M_d and α decrease along the empirical evolution sequence (as n increases).

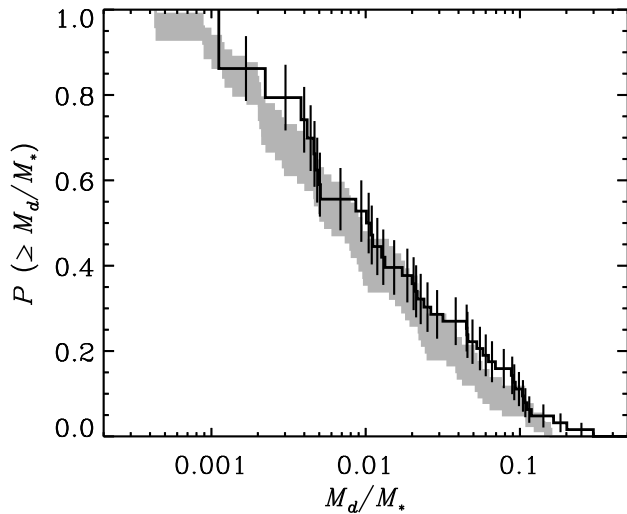


Fig. 7.— The cumulative distributions of the disk-to-star mass ratio for Class II sources in ρ Oph (*lines*) and Taurus (*grayscale*). While the ρ Oph sources appear to generally have slightly larger mass ratios than their Taurus counterparts, two-sample tests on the censored data indicate that the difference is not statistically significant. The median ratios are $\sim 1.0\%$ and 0.8% for ρ Oph and Taurus, respectively.

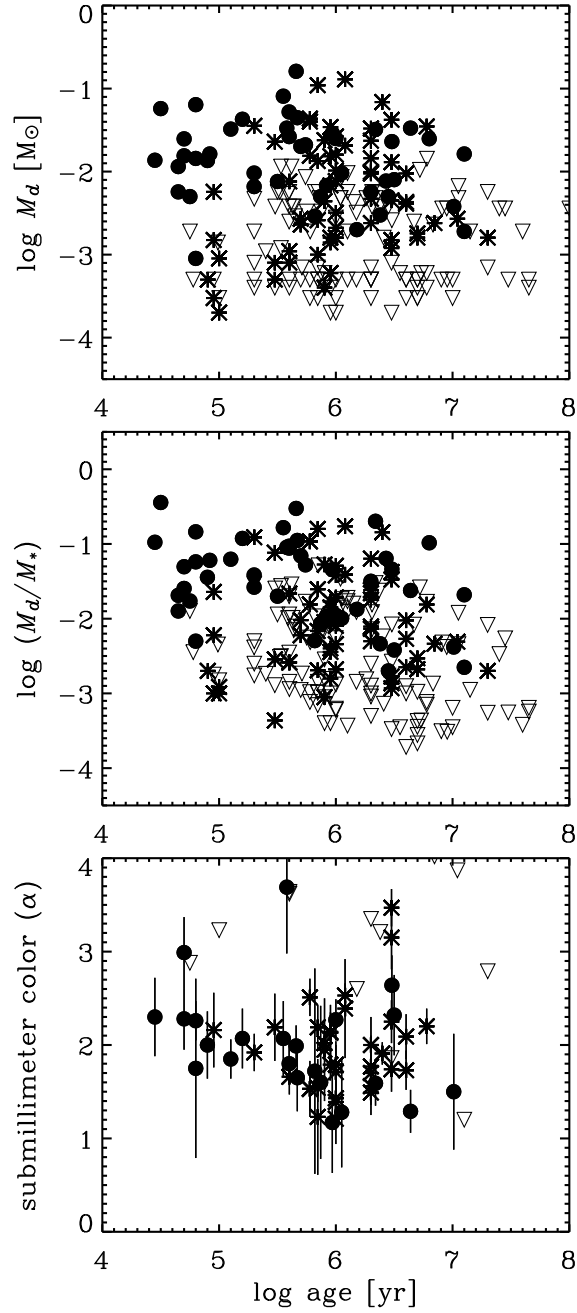


Fig. 8.— Disk masses, disk-to-star mass ratios, and submillimeter colors as a function of the stellar age for the combined ρ Oph (*circles*) and Taurus (*asterisks*) samples. Open triangles are upper limits. Correlation tests on the censored data show that the disk-to-star mass ratio decreases significantly with time, although similar trends for M_d and α are not clear.

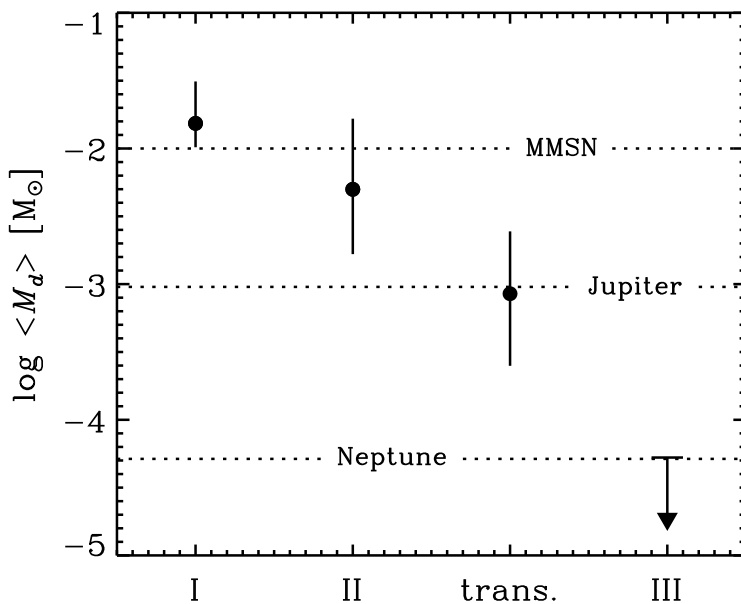


Fig. 9.— Schematic diagram showing the evolution of the median disk masses across the empirical sequence defined by the shape of the infrared SED (see also Table 4). The transition objects (“trans.”) are defined as Class III sources with firm submillimeter detections, and the Class III limit corresponds to the stacking analysis value determined in §4.1. Dashed horizontal lines mark standard reference masses.

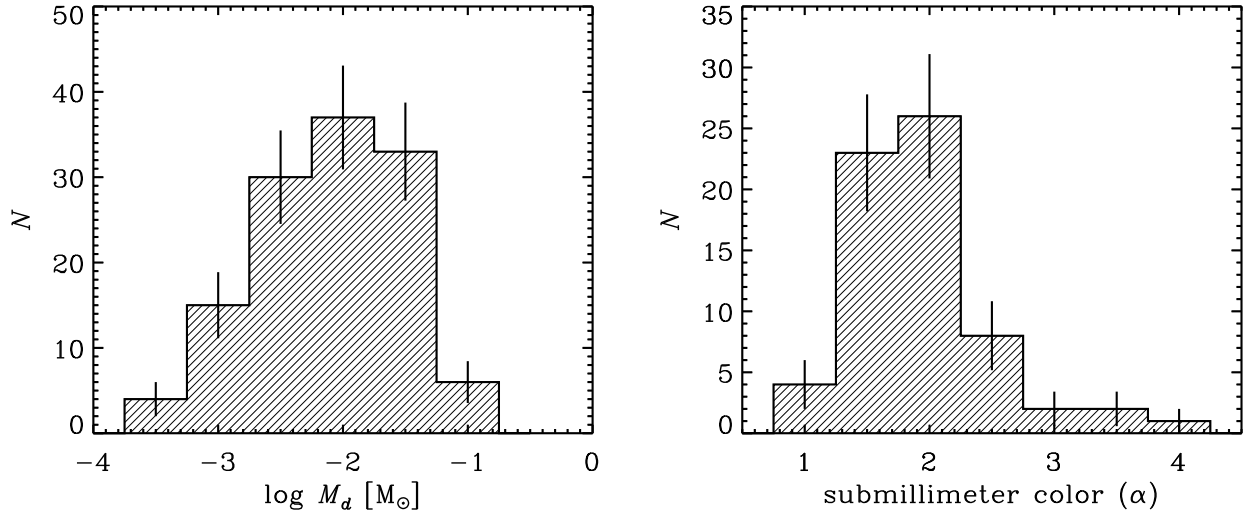


Fig. 10.— The differential distributions of M_d and α for Class II sources that were firmly detected at submillimeter wavelengths in the combined ρ Oph and Taurus surveys. Uncertainties correspond to the counting errors in each bin. These distributions are representative of the known properties of disks that may represent the initial conditions for the planet formation process.

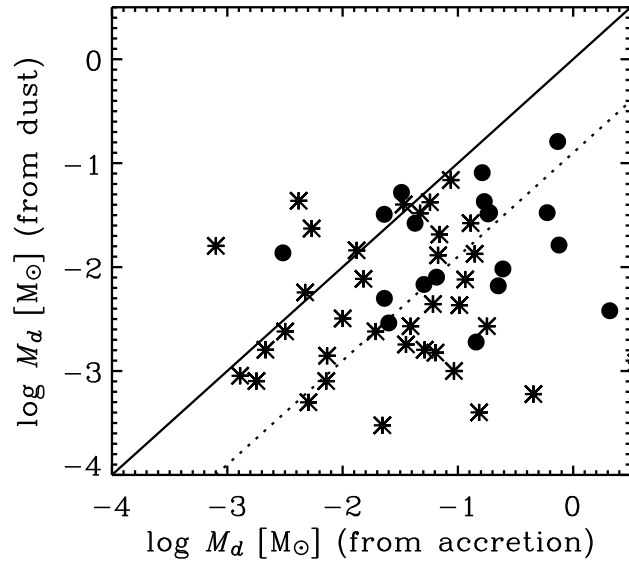


Fig. 11.— A comparison of disk masses inferred in two independent ways for ρ Oph (*circles*) and Taurus (*asterisks*) Class II disks. The abscissa uses gas accretion rates from optical/infrared spectra and some assumptions about the accretion history ($M_d \approx 2t_*\dot{M}$; Hartmann et al. 1998; Natta et al. 2006) and the ordinate the dust masses described in §3.1 and Paper I. The solid line marks the expected behavior if the values were equal. The dotted line bisects the sample, and indicates that dust masses underestimate the accretion masses by nearly an order of magnitude. Particle growth up to meter size scales may explain the discrepancy, due to a significant over-estimate of the disk opacity.